

# WIND TUNNEL INVESTIGATION ON UNSTEADY VORTEX FLOW OVER A HYPERSONIC DELTA GLIDER IN SUBSONIC REGIME

Salaheldin Omar and Salem Abossmaï\*

Talent and Technology Creativity Unit, University of Tabuk, Saudi Arabia,

\* Aeronautical Engineering Dept., Libyan Air Academy, Misrata, Libya

Email: Salaheldin.omar@outlook.com

## المخلص

هذا البحث يتعلق بقياسات في نفق الهواء لمركبات السرعة الثلاثة الغير مستقرة الخاصة بتدفق الهواء الدوامي الشكل في المجال تحت الصوتي فوق المركبات الطائرة الانزلاقية الفرط صوتية ذات الشكل دلتا. القياسات تمت باستخدام مسبار السلك الساخن من النوع ثابت درجة الحرارة تم قياسها في نفق رياح دون سرعة الصوت عند زوايا هجوم مختلفة. تم تثبيت مسبار السلك الساخن على منظومة متحركة على ثلاثة محاور متعامدة متصلة بالحاسب الذي يتم برمجته ليثبت بدقة عند جميع نقاط القياس المحددة مسبقا والتي تشكل مقطع عرضي في الهواء فوق سطح المركبة الطائرة. تم مقارنة موقع محور الدوامة على جانبي الطائرة المتحصل عليه من هذه النتائج مع موقعها بناء على اظهار حركة الهواء باستخدام مقاطع الليزر والتي تم نشرها مسبقا من الباحث واطهرت اختلاف عند زاوية الهجوم العالية. تم مقارنة هذه النتائج ايضا مع نتائج توزيع الضغط السطحي عند مقاطع مختلفة تم نشرها في بحث مسبق للباحث واطهرت انهيار مبكر للدوامتان في القياسات باستخدام السلك الساخن عند زاوية الهجوم العالية (30 درجة) وذلك بسبب التأثير التداخلي لمسبار السلك الساخن المتواجد داخل الدوامتان ومحورهما مع الهواء داخل الدوامتان وبالتبعية اعاقه تدفق الهواء من داخل الدوامتان لخارجهما في اتجاه سريان الهواء وبخاصة في اسطوانة محور كل دوامة مما سرع بحدوث انهيار للدوامتان عند زاوية هجوم ثلاثون درجة في حين اظهرت نتائج قياس الضغط السطحي وكذلك صور اظهار حركة الهواء في الدوامتان عند نفس المقطع وزاوية الهجوم عدم وجود انهيار للدوامتان وان هذا الانهيار بدا فعليا عند زوايا هجوم اعلى من هذه الزاوية. تزداد هذه الاختلافات بزيادة زاوية الهجوم بسبب تحرك موقع انهيار الدوامة (الذي يحدث خلف المركبة الطائرة) الى الامام عكس اتجاه سريان الهواء في اتجاه الحافة الخلفية لجناح المركبة الطائرة وظهور منطقة تدرج ضغطي مناوي فوق المنطقة الخلفية للجناح وبسبب ازدياد انحناء القلب الاسطواني المصمت للدوامة.

تزداد اعاقه تدفق الهواء داخل الدوامات المخروطية فوق سطح الجناح الدلتا بسبب وجود مسبار السلك الساخن في مجالها مع زيادة زاوية الهجوم للمركبات الطائرة ومع تحرك مقطع القياس تجاه الحافة الخلفية للجناح الدلتا ويؤدي ذلك بالتبعية الى تشويه النتائج وعدم موثوقيتها والى انهيار مبكر للدوامات عند زوايا الهجوم العالية وينصح في هذه الحالة باستخدام طرق قياس لا تتداخل مع مسار تدفق الهواء مثل القياس باستخدام الليزر.

## ABSTRACT

In this wind-tunnel investigation, unsteady 3-D velocity components over a hypersonic delta glider have been measured in subsonic wind tunnel using a constant temperature hot-wire probe at different angles of attack. The effect of the intrusive hot-wire probe on the vortex core and the vortex structure has been predicted at angles of attack over 25 degree and  $x/Cr=0.9$  resulting in an early vortex breakdown. Stream wise, vertical and lateral root-mean-square velocity components over the wing have been presented. The acquired data are correlated to the surface-pressure data and the laser-light-sheet results published by the author. The lateral location of the vortex subcore has

been predicted using the data of the hot-wire measurements, the surface pressure measurements, and the flow visualization, while the vertical location of the vortex subcore axis over the wing upper surface is predicted using the data of hot-wire measurements and the flow visualization. The predicted experimental data using the intrusive hot-wire probe reflects obvious interferences and deviations from those obtained using surface pressure transducers. These differences increase by increasing the angle of attack and by moving downstream close to the trailing edge due to the upstream movement of the adverse pressure region and to the kinking of the vortex axis over the rear part of the wing. Based on these results, it is advised to avoid using intrusive probes to investigate vortex flow because of its distortion effect on the vortex structures and the early vortex breakdown, and using instead nonintrusive methods as Laser Doppler Velocimetry (LDV).

**KEYWORDS:** Wind Tunnel; Hypersonic Glider; Delta Wing; Vortex Flow; Vortex Breakdown; Hot-wire Measurements; Velocity Components; Surface-Pressure Measurements;

## INTRODUCTION

### Vortex Formation

The free stream flow ahead of a delta wing is splitted into upper and lower streamlines which rejoin at the separation line along the wing leading edge forming separated free shear layer of two separated adjacent streams of different velocities with the lower streamlines of higher velocity initiating laminar small waves inducing vertical velocities and perturbations forming discrete vortices, Figure (1a).

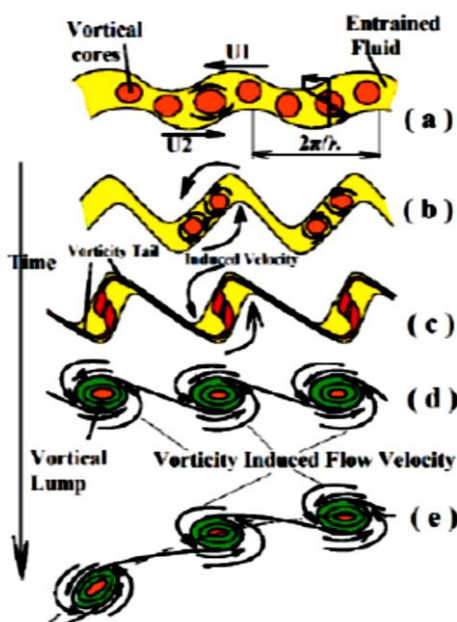


Figure 1: vorticity formation [1]

The free shear layer thickness increases and mixes gradually by moving away, Figure (1b) initiating big spiral vortices due to the Kelvin-Helmholtz instability forming periodically fatter and thinner regions as shown in Figure (1c) forming spirals and triggering the pairing process and consequentially amplifying spatial and irregularities in the vortex structure forming rotating vortex lumps in the interfacial region of the free shear layer Figure (1d) and Figure (2). The free shear layer rolls up into a vortex core as

shown in Figures (1d and 1e, 2, and 3) of wind tunnel smoke and laser-light-sheet flow visualization over sharp edged delta wing after Omar [2]. The primary vortex can be divided, after Earnshaw [3], into three regions, namely, the free shear layer, the rotational core, and viscous subcore as shown in Figure (2).

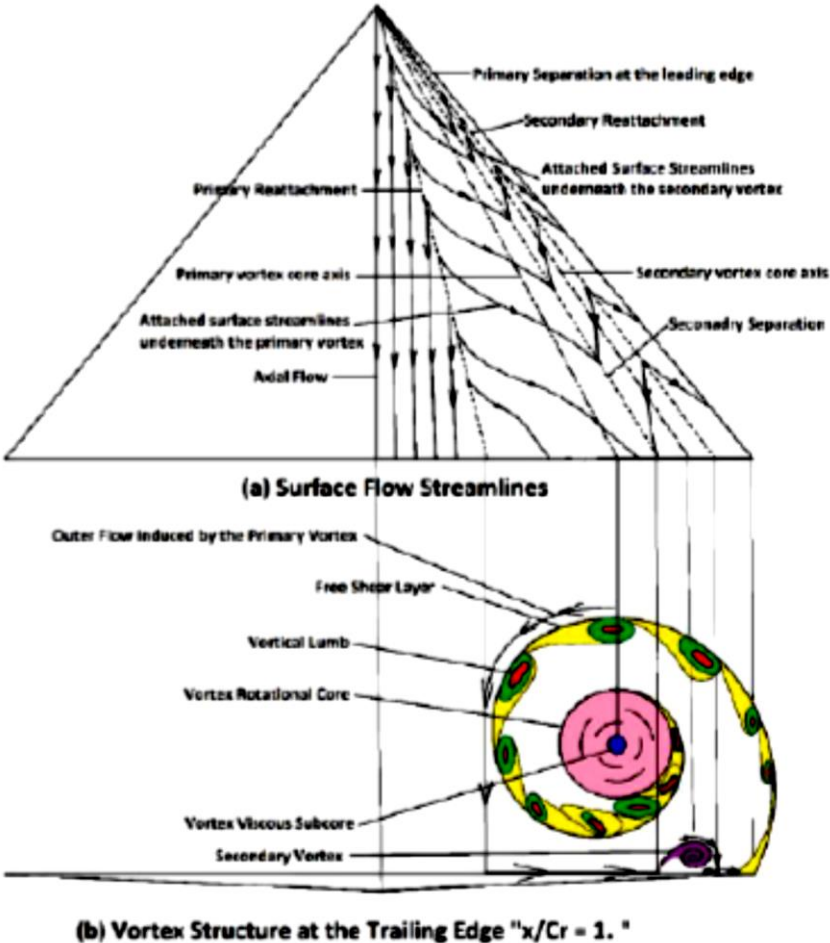


Figure 2 vortex flow over delta wing [1]



Figure 3: primary vortex [2]

The free shear layer generated at the leading edge rolled up forming the primary vortex induces the outer flow of the primary vortex to reattach on the leeward side of the delta wing and is continually providing the boundary layer after the reattachment line

with fresh air of high energy as illustrated in figure after Omar [2]. The reattached flow moves from the reattachment line outboard toward the leading edge until it separates at the secondary separation line somewhere between the axis of the primary vortex and the leading edge in dependence of the flow condition “laminar/turbulent” forming the secondary vortex. A tertiary vortex may be initiated underneath the secondary vortex with a rotation in the same sense as the primary vortex.

**Vortex Breakdown**

Vortex breakdown is a rush sharp deformation of the structure of the vortex core and dominance of asymmetric flow around the vortex axis after Sarpkaya [4] or disturbances accompanied by deceleration of the vortex internal flow along the vortex axis until reaching a stagnation condition forming reversed flow, after Leibovich [5] and Garg A. and Leibovich [6], in dependence of the external pressure gradient and the vorticity convection along the vortex axis after Schade H., Michalke, A. (1962) and Hall [8], and in dependence of the magnitude of the vortex swirling, as an indication of the vorticity shedded in the rolled up free shear layer, the external pressure gradient and the vorticity convection along the axis of the vortex Schade H., Michalke [7]. Raising the rate of generation of the vortices shedded in the vortex sheet to a level exceeding the rate of convection of these vortices downstream along the vortex axis increasing the concentrated vortices until exceeding the maximum vortices per unit area "critical vortices concentration". The interactions among the vortex-outer-core spirals along with the formation of a stagnation point on the viscous subcore axis result in a vortex breakdown in the form of spiral-form or bubble-form vortex breakdown shown in Figure (4). Vortex breakdown spreads the vortices over a wider region redistributing excessive vortices in the region aft the vortex-breakdown location resulting in a reduction in the vorticity concentration inside the vortex sheet. More details are available in Omar [1, 11].

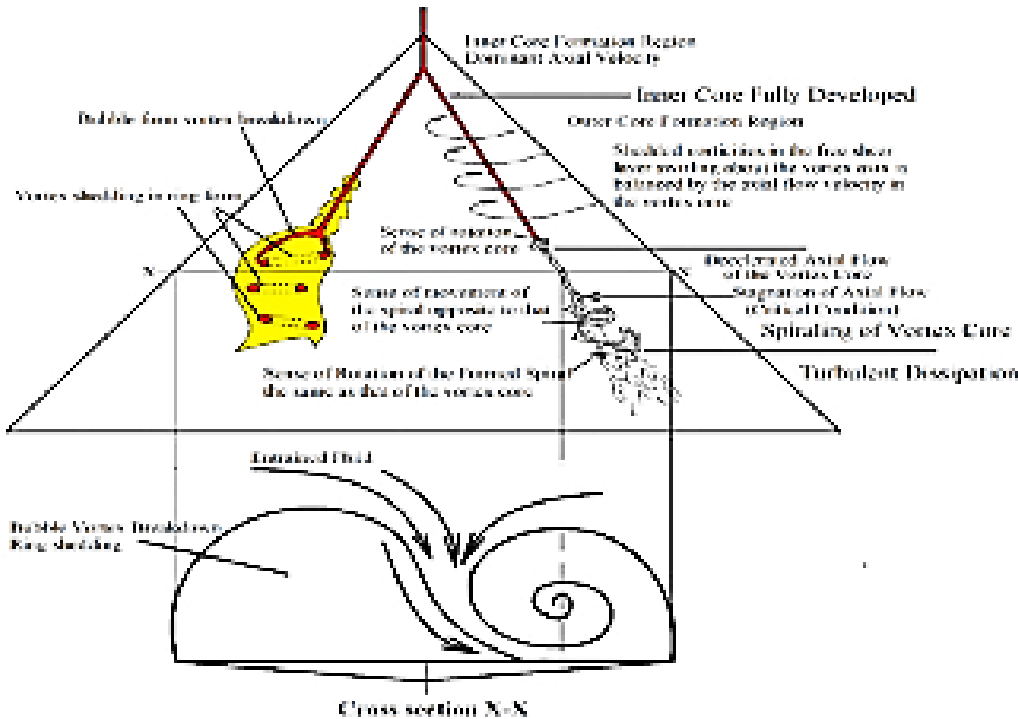


**Figure 4: Vortex breakdown [1]**

## EXPERIMENTAL SETUP

Acquiring velocity components of the flow can be achieved using hot wire probes. Hot wire probe measurements have intrusive nature, the probe interferes with and modifies the flow being measured. They are affected also by the vibrations, which should be minimized for unsteady measurements after Jorgensen [9] and Yavuzkurt [10]. Intrusive constant temperature anemometer “CTA” is used in this investigation in TUM subsonic wind tunnel of 1.5m diameter, 55m/s maximum speed and 0.3 turbulence intensity, Figure (6 and 7), to predict the unsteady velocity components over a hypersonic delta glider in subsonic regime. The light-weight stiff carbon-fiber test model used in this investigation has an aspect ratio  $AR = 1$ , sweep back angle  $\Lambda_{LE} = 76^\circ$ , a 670mm length, 335mm span, and 57.2mm maximum thickness as shown in Figure (5a, 5b and 5b). The hot-wire probes used in this investigation are x probes, which are oriented perpendicular to each other and at an angle of 45 degrees to the mean flow. In this configuration each wire sensor is cooled differently depending on the direction and magnitude of the flow. This enables a unique voltage pair, one for each wire, to be given for each velocity and angle. The X-wire probe is only able to measure two components of velocity. In order to fully predict all three velocity components (u, v, w), the probe is rotated around its axis by 90 degrees to adjust the wire plane against the main flow direction. In this context, two traverse sweeps are necessary for each plane to obtain all three components of velocity. With the probe oriented in the horizontal direction the x and y components are acquired, while orienting the probe in the vertical position allows the prediction of the x and z components. By analyzing the acquired data, the true stream wise velocity is given by the vertical orientation of the probe allowing the prediction of both horizontal and vertical stream wise velocity components as well as the lateral and vertical components. For this purpose, a DISA probe, type 55A32, which has two platinum-plated tungsten wires of 1.2mm long and  $5\mu\text{m}$  thick with X-configuration arrangement, has been used. The total length of the probe is 68 mm with a diameter of 7mm. The calibration of the hot-wire probes is a computer aided fully automated procedure developed based on a velocity and flow angle dependent temperature correction. The calibration of each probe requires about 7 hours to take place. The probes were mounted on a computer-controlled three-axis traverse system. The sampling frequency was 3kHz with 19200 samples for each channel. A low-pass filter of 1kHz has been used. three degree of freedom traversing system of 0.1mm accuracy is used to hold the hot wire probe at all predefined measurement points at two test sections perpendicular to the leeward side of the wing of  $x/Cr=0.5$  and 0.9 for different angles of attack of 12.5, 25 and 30 degrees and free-stream velocity of 37m/s. A static and dynamic calibration for the hot wire was made to allow the conversion of the measured data of the hot wire probe to their corresponding flow velocity components. The accuracy of the measured velocity components by the used constant temperature hot wire probe, which lies within 3% after Yavuzkurt and Omar [10, 11], is affected directly by the accuracy of the used hot wire anemometer, accuracy of the calibration of the probe, accuracy of the traversing system, accuracy of the measured temperature, and the effect of the intrusive hot wire probe on the vortex flow structure and vortex breakdown.



Figure 5a: test model in wind tunnel 2



Figure 5b: Wind tunnel 2

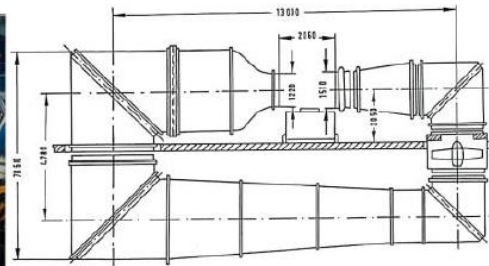


Figure 5c: Wind tunnel 2

The results are correlated to the predicted surface pressure measurements acquired in a subsonic wind tunnel of 1.2m diameter, 72m/s maximum velocity and 0.2 turbulence as shown in Figure (5a, b and c). A total number of 70 Kulite piezo resistive full differential miniature pressure transducers of the type CQ-107-093-5D as shown in Figure (8) are integrated in the leeside surface of the test model as shown in Figure (9). More details are available in Omar [1].

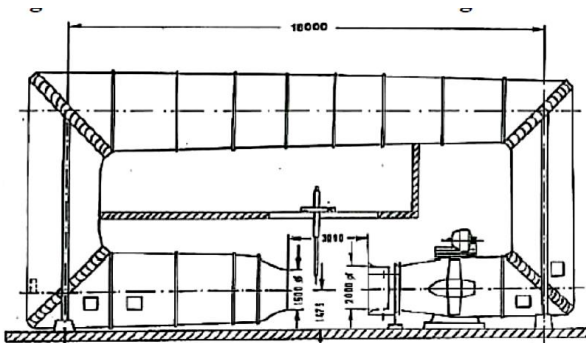


Figure 6: Wind tunnel 1

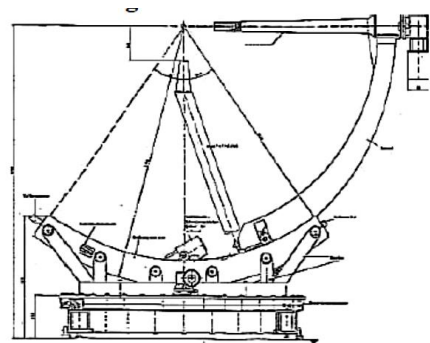


Figure 7: support system for wind tunnel 1



**STANDARD VERSION MINIATURE PRESSURE TRANSDUCER**

**XCQ-093 SERIES**

- Ideal For Turbine Engine Probes and Wind Tunnel Applications
- 50 Year History Of Successful Applications In Wind Tunnel And Flight Test Programs
- Patented Silicon on Silicon Integrated Sensor **VIS®**
- Size And Shape Ideal For Incorporation In User Designed Probes
- Excellent Static And Dynamic Performance

The XCQ-093 Series allows for a very rugged package suited for probes, pressure rakes and other similar test set-ups. This transducer is well suited for both dynamic and static pressure measurements in benign or harsh environments.



Kulite recommends the KSC-2 signal conditioner to maximize the measurement capability of the XCQ-093 transducer.

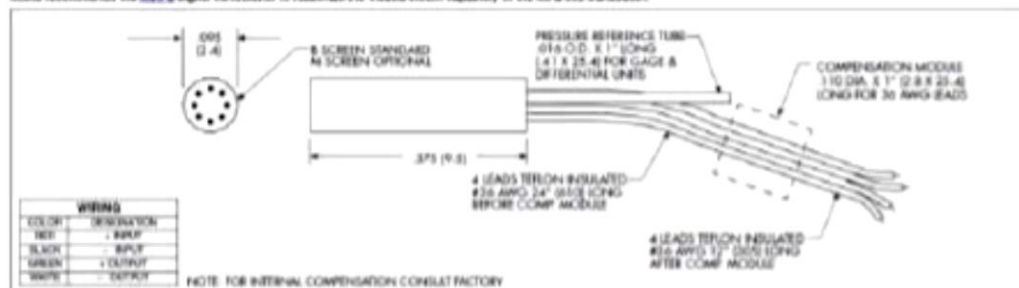


Figure 8: Kulite miniature pressure sensor

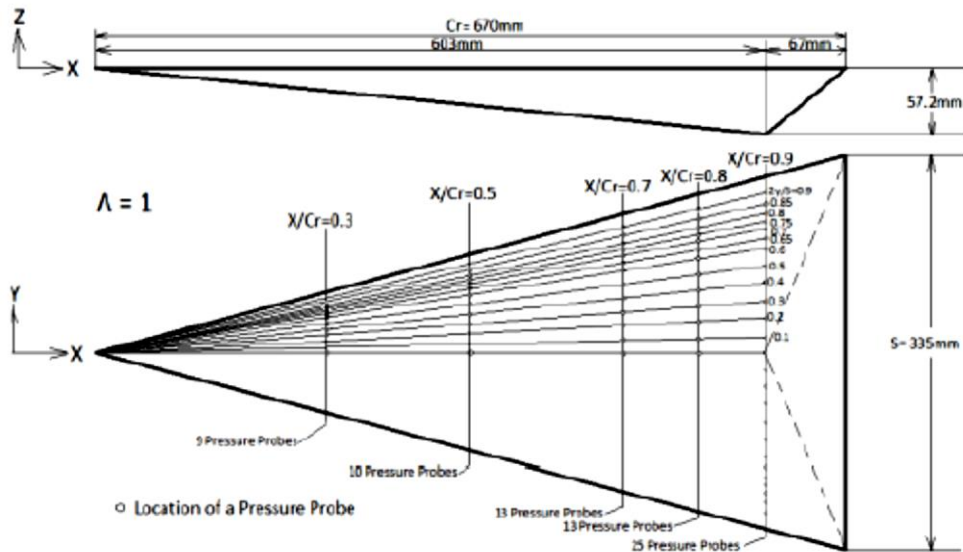


Figure9: dimensions and test sections of test model

## RESULTS AND DISCUSSION

The acquired velocity components predicted using the hot-wire anemometer are presented in the form of stream wise velocity vector “ $u/U$ ”, lateral velocity components “ $v/U$ ”, vertical velocity components “ $w/U$ ”, cross-flow velocity vectors, root mean square values of stream wise velocity vector “r.m.s. ( $u/U$ )”, lateral velocity vectors “r.m.s. ( $v/U$ )” and vertical velocity vectors “r.m.s. ( $w/U$ )” for  $12.5^\circ$  angle of attack and  $x/Cr=0.5$  are shown in Figures (10, 11, 12 and 13) sequentially and in Figures (14, 15, 16 and 17) for  $x/Cr=0.9$ . They are presented in Figures (18, 19, 20 and 21) for  $25^\circ$  angle of attack and  $x/Cr=0.5$  and in Figures (22, 23, 24 and 25) for  $x/Cr=0.9$ . At  $30^\circ$  angle of attack and  $x/Cr=0.5$ , these values are shown in Figures (26, 27, 28 and 29) and for  $x/Cr=0.9$  and in Figures (30, 31, 32 and 33) sequentially. The root mean square value of stream wise velocity r.m.s. ( $u/U$ ) at  $x/Cr=0.5$  and  $x/Cr=0.9$  are presented in colors for  $12.5^\circ$ ,  $25^\circ$ , and  $30^\circ$  angles of attack in Figures (34, 35 and 36) sequentially. The lateral and vertical location of the primary-vortex viscous subcore over the wing at different downstream cross sections “ $x/Cr$ ” and angles of attack based on hot-wire data are shown in Figures (37-40, 43-46, 49-56, 59-62, and 65-68). The root mean square values of vertical velocity components “r.m.s. ( $w/U$ )” for  $x/Cr=0.5$  and  $0.9$  and angles of attack of  $12.5^\circ$ ,  $25^\circ$  and  $30^\circ$  are shown in Figures (41, 42, 47, 48, 57, 58, 69 and 60) with comparison with data from surface pressure measurements and laser-light-sheet flow visualization shown in Figures (72-76).

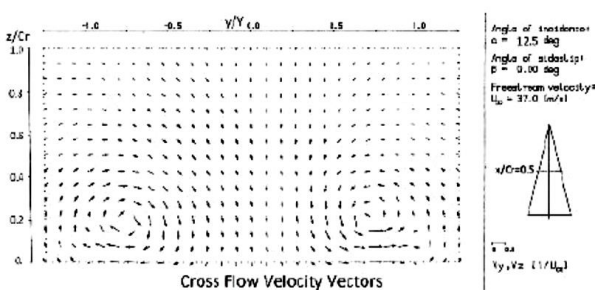


Figure10: Cross flow velocity,  $x/Cr=0.5$ ,  $\alpha = 12.5^\circ$

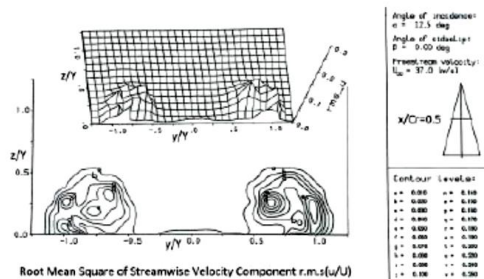


Figure 11 r.m.s. r.m.s. ( $u/U$ ),  $x/Cr=0.5$ ,  $\alpha = 12.5^\circ$

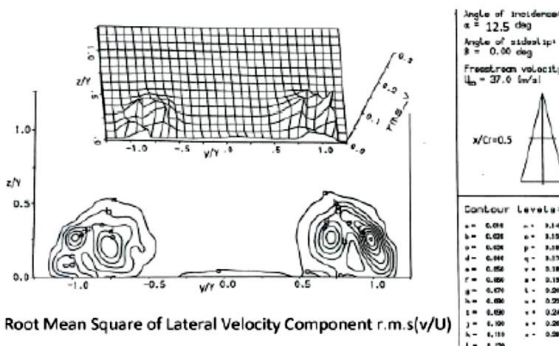


Figure 12: r.m.s. (v/U),  $x/Cr=0.5$ ,  $\alpha=12.5^\circ$

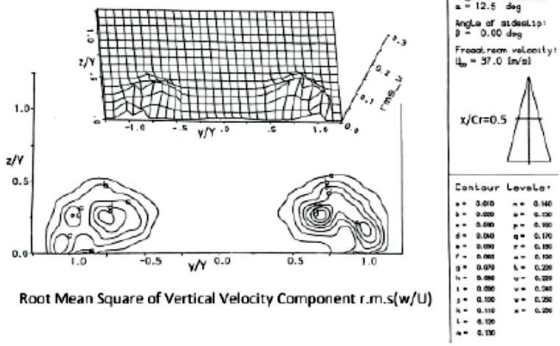


Figure 13: r.m.s. (w/U),  $x/Cr=0.5$ ,  $\alpha=12.5^\circ$

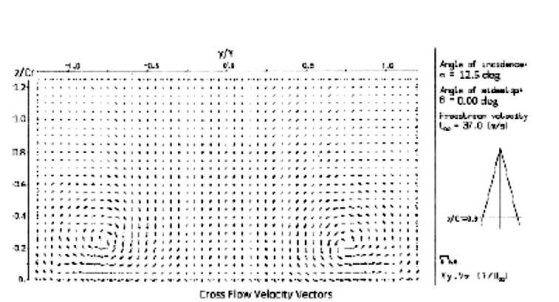


Figure 14: Cross flow velocity,  $x/Cr=0.9$ ,  $\alpha=12.5^\circ$

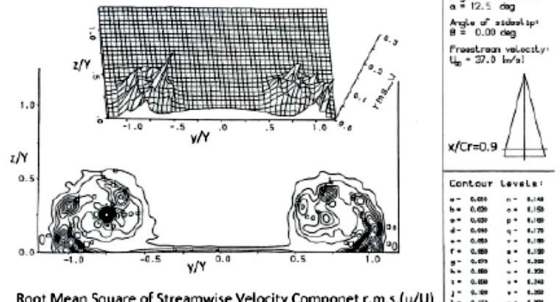


Figure 15: r.m.s. (u/U),  $x/Cr=0.9$ ,  $\alpha=12.5^\circ$

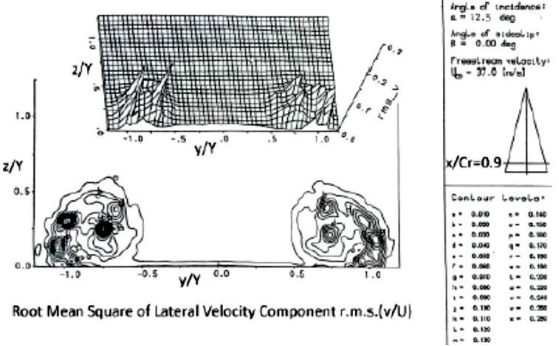


Figure 16: r.m.s. (v/U),  $x/Cr=0.9$ ,  $\alpha=12.5^\circ$

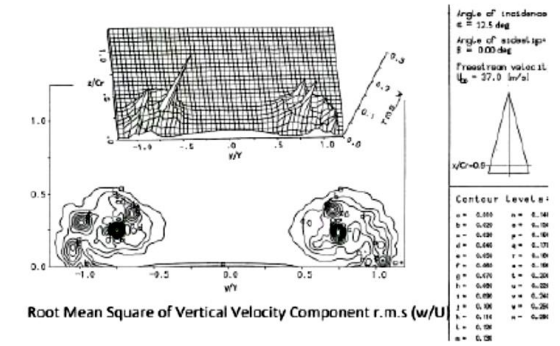


Figure 17: r.m.s. (w/U),  $x/Cr=0.9$ ,  $\alpha=12.5^\circ$

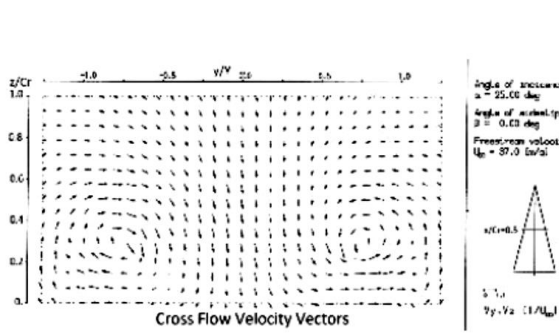


Figure 18: cross flow velocity,  $x/Cr=0.5$ ,  $\alpha=25^\circ$

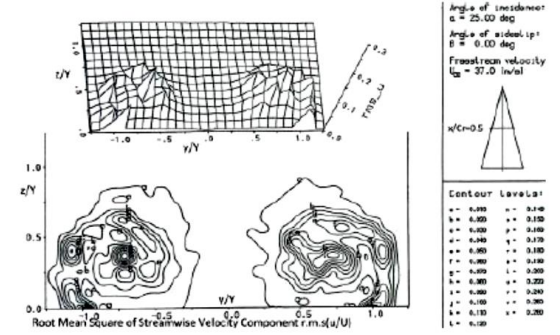


Figure 19: r.m.s. (u/U),  $x/Cr=0.5$ ,  $\alpha=25^\circ$

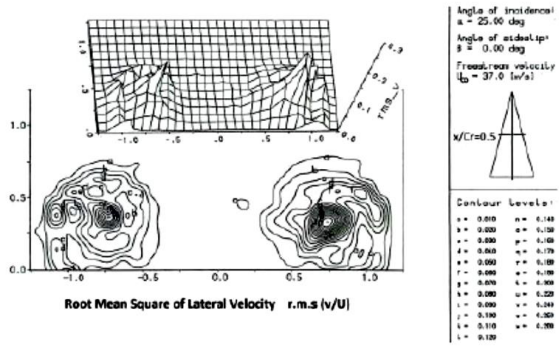


Figure 20: r.m.s. (v/U), x/Cr=0.5,  $\alpha = 25^\circ$

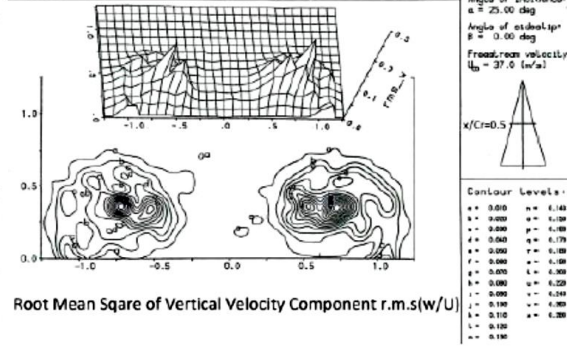


Figure 21: r.m.s. (w/U), x/Cr=0.9,  $\alpha = 25^\circ$

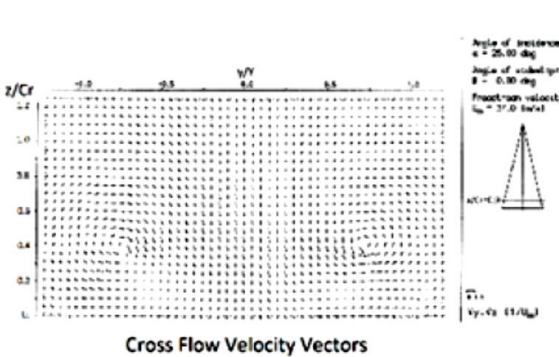


Figure 22: cross flow velocity, x/Cr=0.9,  $\alpha = 25^\circ$

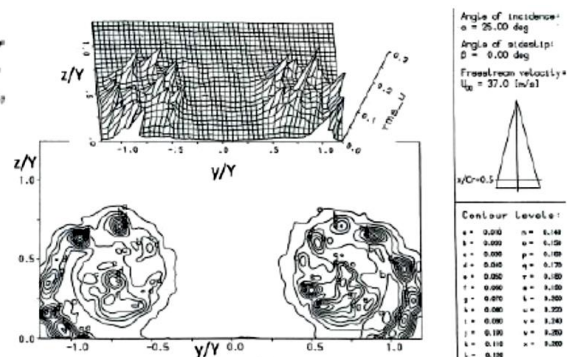


Figure 23: r.m.s. (u/U), x/Cr=0.9,  $\alpha = 25^\circ$

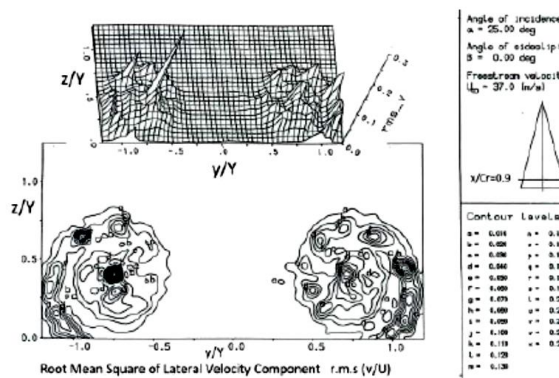


Figure 24: r.m.s. (v/U), x/Cr=0.9,  $\alpha = 25^\circ$

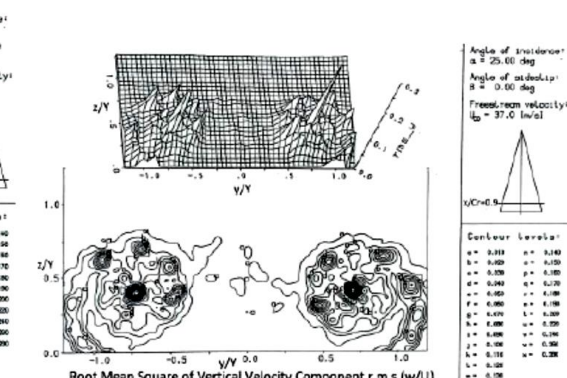


Figure 25: r.m.s. (w/U), x/Cr=0.9,  $\alpha = 25^\circ$

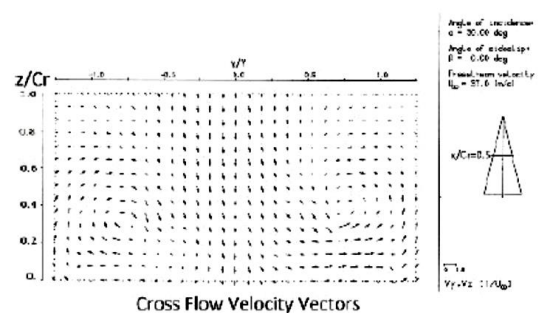


Figure 26: cross flow velocity, x/Cr=0.5,  $\alpha = 30^\circ$

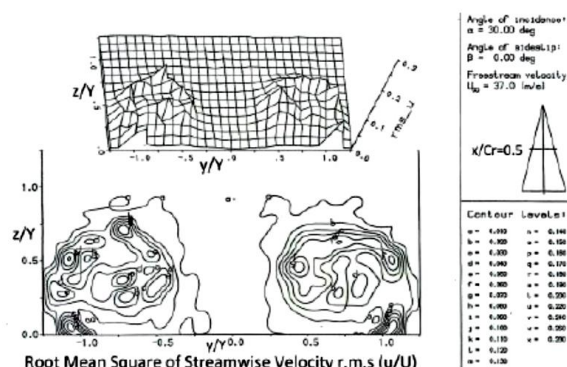


Figure 27: r.m.s. (u/U), x/Cr=0.5,  $\alpha = 30^\circ$

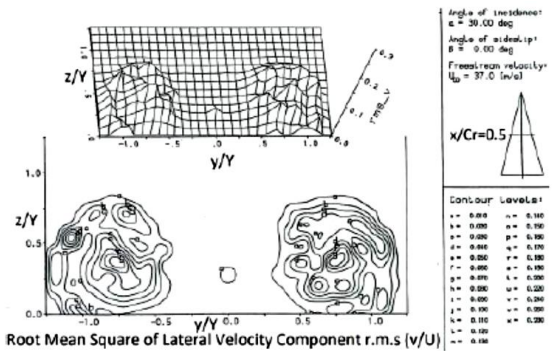


Figure 28: r.m.s. (v/U), x/Cr=0.5,  $\alpha = 30^\circ$

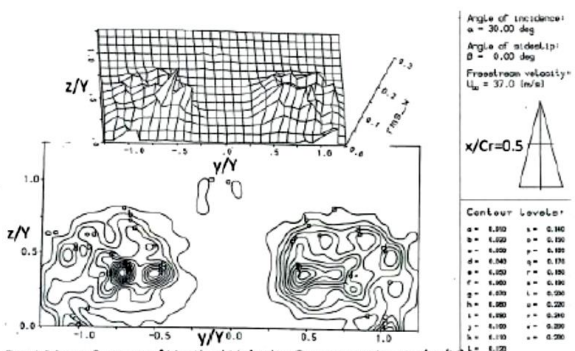


Figure 29: r.m.s. (w/U), x/Cr=0.5,  $\alpha = 30^\circ$

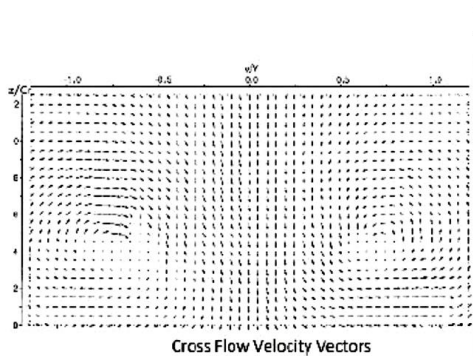


Figure 30: cross flow velocity, x/Cr=0.9,  $\alpha = 30^\circ$

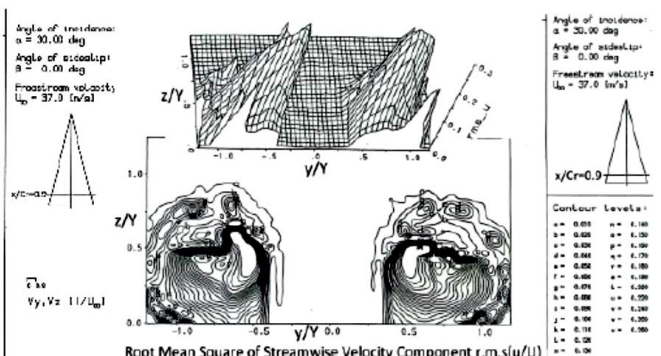


Figure 31: r.m.s. (u/U), x/Cr=0.9,  $\alpha = 30^\circ$

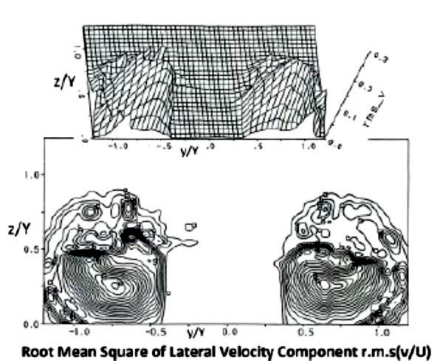


Figure 32: r.m.s. (v/U), x/Cr=0.9,  $\alpha = 30^\circ$

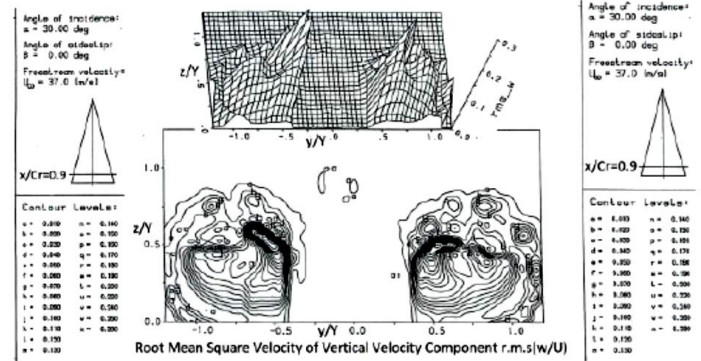


Figure 33: r.m.s. (w/U), x/Cr=0.9,  $\alpha = 30^\circ$

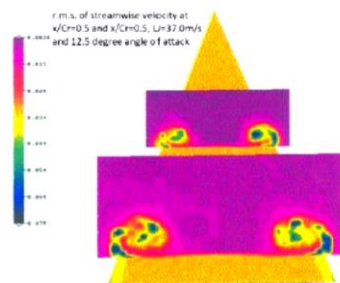


Figure 34: r.m.s. (u/U) for 12.5° angle of attack

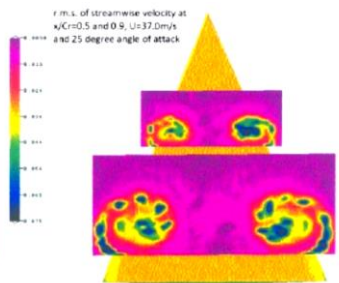


Figure 35: r.m.s. (u/U) for 25° angle of attack

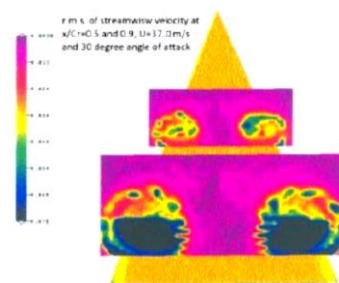


Figure 36: r.m.s. (u/U) for 30° angle of attack

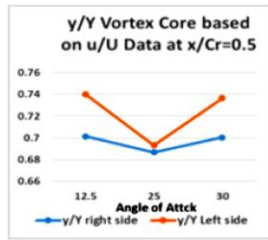


Figure 37: y/Y (vortex core), x/Cr=0.5

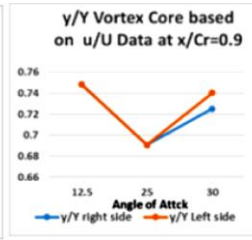


Figure 38: y/Y (vortex core), x/Cr=0.9

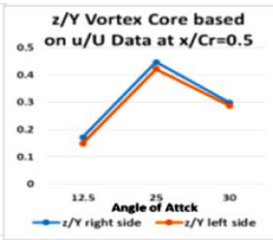


Figure 39: z/Y (vortex core), x/Cr=0.5

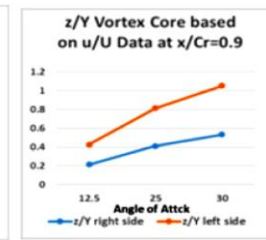


Figure 40: z/Y (vortex core), x/Cr=0.9

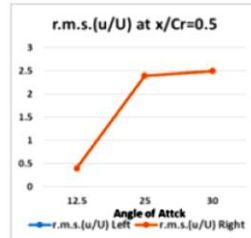


Figure 41 r.m.s. (u/U), x/Cr=0.5

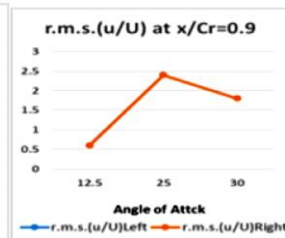


Figure 42 r.m.s. (u/U), x/Cr=0.9

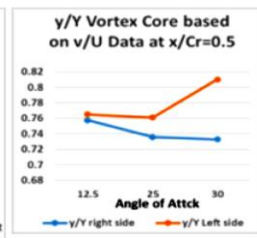


Figure 43 y/Y (vortex core), x/Cr=0.5

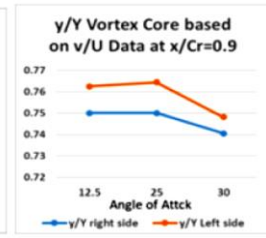


Figure 44 y/Y (vortex core), x/Cr=0.9

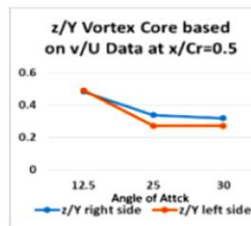


Figure 45: z/Y (vortex core), x/Cr=0.5

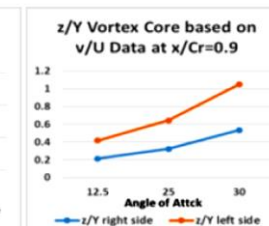


Figure 46: z/Y (vortex core), x/Cr=0.9

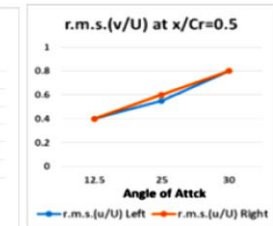


Figure 47: r.m.s. (v/U), x/Cr=0.5

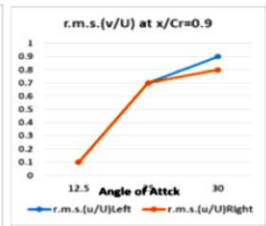


Figure 48: r.m.s. (v/U), x/Cr=0.9

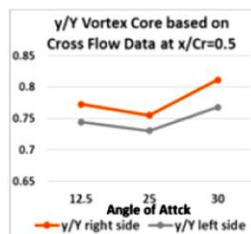


Figure 49 y/Y (vortex core), x/Cr=0.5

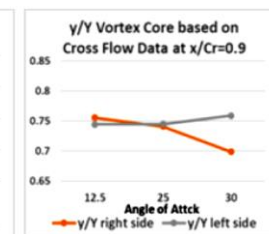


Figure 50 y/Y (vortex core), x/Cr=0.9

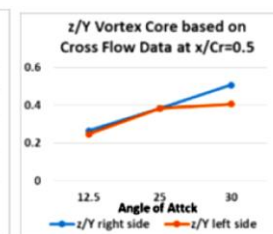


Figure 51: z/Y (vortex core), x/Cr=0.5

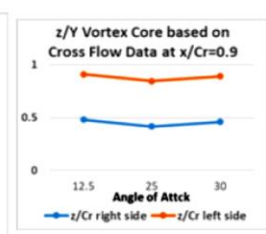


Figure 52: z/Y (vortex core), x/Cr=0.9

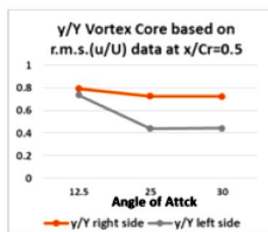


Figure 53: y/Y (vortex core), x/Cr=0.5

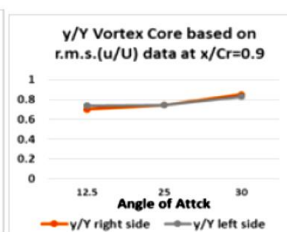


Figure 54: y/Y (vortex core), x/Cr=0.9

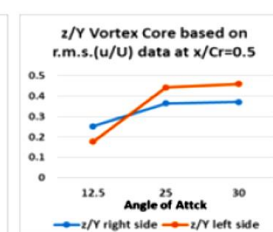


Figure 55: z/Y (vortex core), x/Cr=0.5

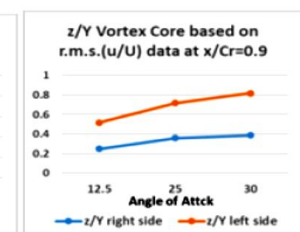


Figure 56: z/Y (vortex core), x/Cr=0.5

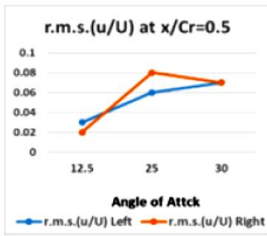


Figure 57: r.m.s. (u/U), x/Cr=0.5

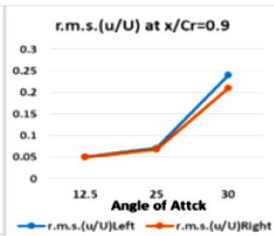


Figure 58: r.m.s. (u/U), x/Cr=0.9

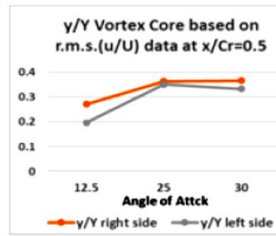


Figure 59: y/Y (vortex core), x/Cr=0.5

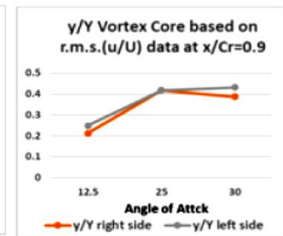


Figure 60: y/Y (vortex core), x/Cr=0.9

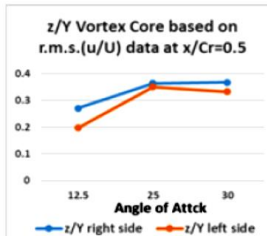


Figure 61: z/Y (vortex core), x/Cr=0.5

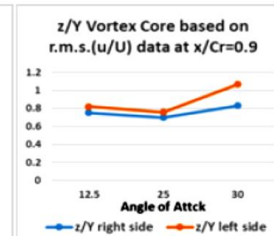


Figure 62: z/Y (vortex core), x/Cr=0.5

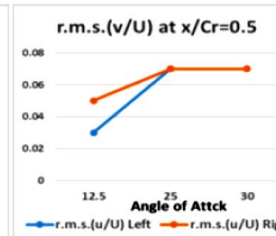


Figure 63: r.m.s. (v/U), x/Cr=0.5

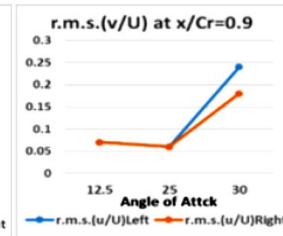


Figure 64: r.m.s. (v/U), x/Cr=0.5

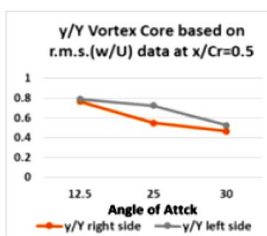


Figure 65: y/Y (vortex core), x/Cr=0.5

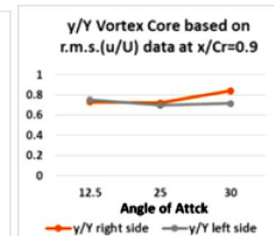


Figure 66: y/Y (vortex core), x/Cr=0.5

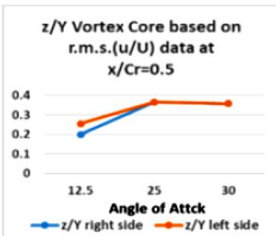


Figure 67: z/Y (vortex core), x/Cr=0.9

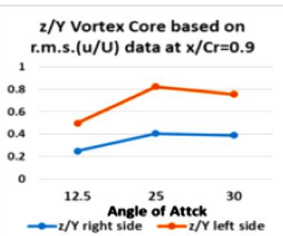


Figure 68: z/Y (vortex core), x/Cr=0.9

The results of the surface-pressure measurements indicate that the axis of the primary vortex moves laterally to the wing longitudinal symmetrical axis by increasing the angle of attack up to  $35^\circ$  as shown in Figure (72) and moves vertically away from the wing surface, based on data of laser-light-sheet flow visualization Figure (75), by increasing the angle of attack up to  $45^\circ$ , but, based on the hot wire data, the vortex axes is located closer to the wing surface than that predicted based on the data of the laser-light-sheet flow visualization.

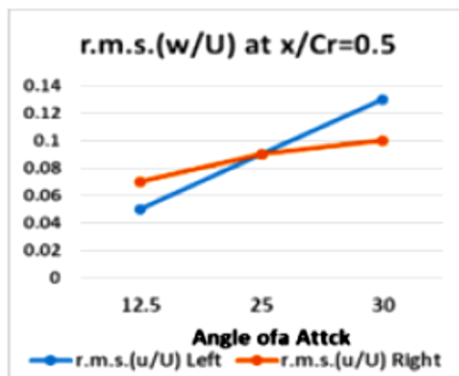


Figure 69: r.m.s. (w/U), x/Cr=0.5

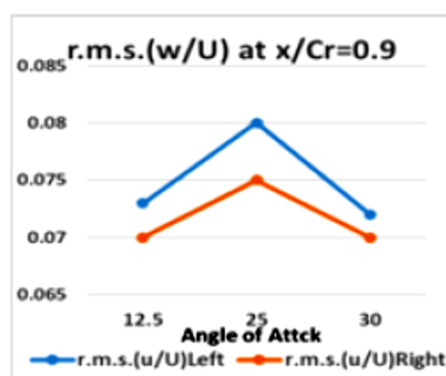


Figure 70: r.m.s. (w/U), x/Cr=0.9

The vertical location of the vortex axes over the wing, predicted based on the hot wire data, is located closer to the wing surface than that predicted based on the data of the laser-light-sheet flow visualization at  $12.2^\circ$  angle of attack Figure (76), it is moved vertically away from the wing surface by increasing the angle of attack up to  $25^\circ$  to a location higher than that predicted based on the data of the laser-light-sheet flow visualization, at  $30^\circ$  angle of attack, it was moved to the opposite direction closer to the wing surface at a location lower than that predicted based on the laser-light-sheet flow visualization data because of the interference and modification of the flow initiated by the intrusive hot-wire anemometer. The disturbing effect of the intrusive hot wire anemometer on the vortex flow is obvious at all angles of attack for both lateral cross sections of  $x/Cr=0.5$  and  $0.9$ , and is enormous at high angles of attack of  $30^\circ$  and above for  $x/Cr=0.9$  close to the area of adverse pressure gradients downstream of the trailing edge of the wing, resulting in early vortex breakdown at  $30^\circ$  angle of attack at  $x/Cr=0.9$  as shown in Figure (36 and 76). The surface pressure distributions at different lateral cross sections on the leeward side of the wing,  $x/Cr$  from  $0.3$  to  $0.9$  Figure (71), indicate that the maximum suction pressure is predicted at  $32^\circ$  angle of attack for the cross sections of  $x/Cr=0.3$  to  $0.7$ , while for  $x/Cr=0.8$  and  $0.9$ , the maximum suction pressure is predicted at  $30^\circ$  angles of attack indicating that the primary vortex over the wing is still healthy showing no sign of vortex breakdown up to  $32^\circ$  angle of attack at all lateral cross sections from  $x/Cr=0.3$  to  $x/Cr=0.9$ .

The lateral locations of the vortex axis over the wing predicted based on data of surface-pressure Figure (72) and laser-light-sheet flow visualization Figure (74) at different angles of attack are identical and they move inboard toward the wing longitudinal symmetrical line by increasing the angle of attack. The lateral location of the vortex axis predicted based on the hot-wire anemometer, listed in Table (1), are located shifted outboard toward the leading edge Figure (73) from their locations predicted based on the surface pressures and the laser-light-sheet flow visualization data due to the interference and modification of the flow initiated by the intrusive hot-wire anemometer.

The data of the acquired surface-pressures indicate increased maximum suction-pressures by increasing the angle of attack up to  $30^\circ$  over all test sections from  $x/Cr = 0.3$  to  $x/Cr = 0.9$  reflecting healthy primary vortex over all test sections with increasing suction pressure by increasing the angle of attack up to  $32.5^\circ$  for all test sections from the  $x/Cr=0.3$  to  $0.9$ , and up to  $35^\circ$  for  $x/Cr=0.3$  and  $0.5$ . Beyond  $32.5^\circ$  angle of attack, the surface suction-pressures decrease at all test sections from  $x/Cr=0.6$  to  $x/Cr=0.9$  and consequently to the trailing edge of the wing. Increasing the angle of attack to  $32.5^\circ$  leads to additional inboard lateral movement of the location of the maximum suction pressure at all test sections to a location at  $y/Y = 0.6$  with an increase in the maximum suction pressure on the leeward side of the wing at all test sections as shown in Figure (71) reflecting the presence of a healthy vortex over all test sections in contradiction with the data acquired from the hot-wire measurements at  $30^\circ$  which indicate a vortex breakdown at  $x/Cr=0.9$ , the reason for that is the disturbance effect of the hot-wire probe on the sensitive vortex flow at such high angle of attack. Surface-Pressure data show increased suction pressure at  $x/Cr = 0.3$  by increasing the angle of attack to  $35^\circ$ , but drops at all other test sections downstream of this location with the maximum drop at  $x/Cr = 0.9$  due to the adverse pressure gradient and the bending of the vortex core upward away from the wing upper surface indicating that the vortex breakdown has already reached the trailing edge and is moving upstream towards the wing apex by increasing the angle of attack.

The wind tunnel laser-light-sheet data indicate that the lateral location of the vortex subcore axis remains unchanged along the downstream position of the vortex over the wing, but it decreases, with different rates, by increasing the angle of attack as shown in Figure (74) after Omar [2]. The Trajectory of the vortex subcore based on the laser-light-sheet flow visualization indicate a continuous inboard movement of the vortex subcore location from  $y/Y=0.9$  at zero-degree angle of attack toward the axis of symmetry of the wing at  $y/Y=0.7$  by increasing the angle of attack up to 10 degrees. It remains at this location by further increase in the angle of attack up to 15°. The vortex subcore location continues its inboard movement to  $y/Y=0.65$  by further increase in the angle of attack up to 20° and remains at this location up to 30°.

**Table 1: Lateral location of the Vortex Subcore**

Angle of Attack (degree)		12.5	25	30
Surface Pressure	y/Y Left	0.7	0.65	0.65
	y/Y Right	0.7	0.65	0.65
Hot Wire Data Cross Flow	y/Y Left	0.74	0.73	0.768
	y/Y Right	0.773	0.755	0.812
Laser Light Sheet	y/Y Left	0.7	0.65	0.65
	y/Y Right	0.7	0.65	0.65

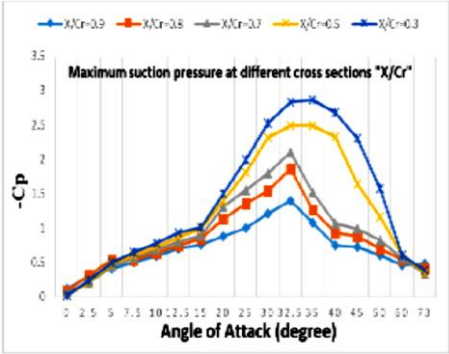


**Figure 71: Max surface suction pressures distribution [1]**

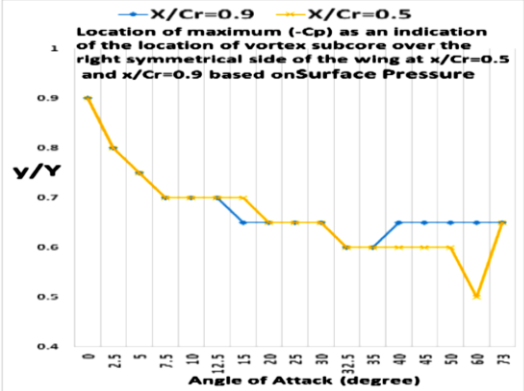


**Figure 72: lateral location of vortex subcore [1]**

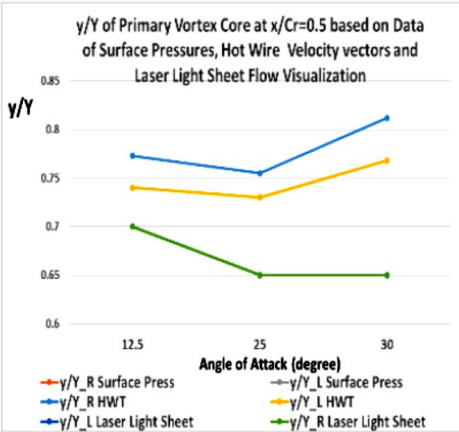


**Figure 73: lateral location of vortex subcore**

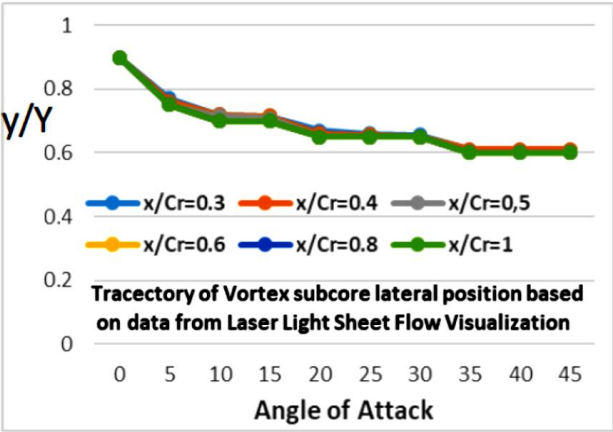


**Figure 74: lateral location of vortex subcore [2]**

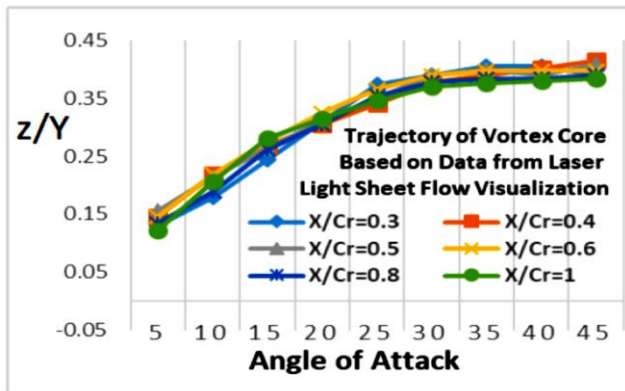


Figure 75: Vertical location of vortex subcore [1]

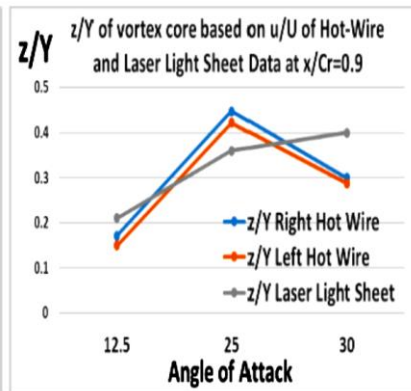


Figure 76: Vertical location of vortex subcore

## SUMMARY AND CONCLUSION

Unsteady 3-D velocity components over a hypersonic delta glider have been measured in subsonic wind tunnel using a constant temperature hot-wire anemometer. Streamwise, vertical and lateral root-mean-square velocity components over the wing have been presented. The acquired data are correlated to the measured surface-pressure data presented by Omar [1] and the laser-light sheet results Omar [2]. The predicted experimental data using the intrusive hot-wire probe reflects obvious interferences and deviations from those obtained using surface pressure transducers. These differences increase by increasing the angle of attack and by moving downstream close to the trailing edge due to the movement of the adverse pressure region upstream and the kinking of the vortex axis over the rear part of the wing. The lateral location of the vortex core axis predicted based on the hot-wire data moves inboard to the wing symmetrical axis by increasing the angle of attack from  $12.5^\circ$  to  $25^\circ$ , but moves in the opposite direction outboard toward the leading edge of the wing by increasing the angle of attack to  $30^\circ$  in contradiction with the acquired data using surface pressures and laser-light-sheet flow visualization which show outboard movement of the vortex subcore axis to the leading edge by increasing the angle of attack up to  $35^\circ$ . The difference in the results at  $30^\circ$  angle of attack is due to the interference effect of the intrusive hot-wire probe on the vortex which have a sensitive structure this high angle of attack due to the upstream movement of the adverse pressure region and the upward kinking of the vortex core resisting the downstream convection of the vortices leading to the instability of the vortex structure and the vortex breakdown. The vertical location of the vortex subcore axis predicted based on the laser-light-sheet flow visualization moves upward away from the wing upper surface by increasing the angle of attack up to  $45^\circ$ , but moves downward closer to the wing surface at  $30^\circ$  angle of attack in contradiction to its location predicted using the flow visualization due to the effect of the intrusive hot-wire probe on the vortex flow which is sensitive to any disturbances at high angles of attack. This investigation clearly indicates the negative effect of the intrusive hot-wire probe on vortex flow especially at high angles of attack leading to wrong results.

## NOMENCLATURES

Cr -	Wing root chord	u -	Streamwise velocity component
Y -	Local wing semis pan	v -	Lateral velocity component
U -	Free stream speed	w -	Vertical velocity component
x -	Local chord-wise distance from wing apex	r.m.s-	Root mean square
y -	Local span-wise distance from wing root	$\alpha$ -	sweep back angle
AR	Aspect ratio	$\Delta_{LE}$	sweep back angle

## REFERENCES

- [1] Omar Salaheldin H. (2020); Wind Tunnel Investigation On Surface-Pressures and Vortex Flowover Delta Wing at High Angles of Attack and Free-Stream Velocities International Journal of Core Engineering ana Management Volume-6, Issue-8, 2020. <http://ijcem.in/archive/volume-6-issue-8-2020-current-issue/>
- [2] Omar Salaheldin H., Adam Saad, Zobi Ashraf, Omar Fatima, Alshamari Fadi (2020); Wind Tunnel Vortex Flow Visualization and Tracking On a Delta Wing at High Angles of Attack, International Journal of Core Engineering and Management Volume-6, Issue-7, 2020. <http://ijcem.in/archive/volume-6-issue-7-2020-current-issue/>
- [3] Earnshaw, P. B (1962). An experimental investigation of the structure of a leading edge vortex. ARC R & M 3281, 1962.
- [4] Sarpkaya, T. (1971). Vortex Breakdown in Swirling Conical Flows, in: AIAA Journal, pp 1792-1799, Vol. 9, No. 9, April 1971.
- [5] Leibovich S. (1979). The structure of vortex breakdown, Annual Review Fluid Mech. 10, 221 (1978).
- [6] Garg, A.K.; Leibovich, S. (1979). Spectral Characteristics of Vortex Breakdown Flow Fields, Physics of Fluids, Vol. 22, No. 11, 1979, pp. 2053-2064. Unsteady Aspects of Leading-edge Vortices RTO-TR-AVT-080 6 -33
- [7] Schade, H.; Michalke, A. (1962) Zur Entstehung von Wirbeln in einer freien Grenzschicht, in: Zeitschrift für Flugwissenschaften, Heft 4/5, pp 147-154, Oktober 1962.
- [8] Hall, M.G. (1972). Vortex breakdown. Ann. Rev. Fluid Mech. 4, 195-218 (1972)
- [9] Jorgensen E (2002) How to measure turbulence with hot wire anemometers. Skovlunde: Dantec Dynamics; 2002. p. 40–4. 462
- [10] Yavuzkurt S. A. (1984) guide to uncertainty analysis of hot wire data. Fluid Eng 1984, 106:181–8.
- [11] Omar Salaheldin H. (2020); A Review on Vortex Flow Over Delta Wings at High Angles of Attack, International Journal of Core Engineering & Management, Volume-6, Issue-9, 2020. <http://ijcem.in/archive/volume-6-issue-9-2020-current-issue/>